Bulletin of the Seismological Society of America, Vol. 85, No. 6, pp. 1576–1590, December 1995

Source Parameters of the 23 April 1992 *M* 6.1 Joshua Tree, California, Earthquake and Its Aftershocks: Empirical Green's Function Analysis of GEOS and TERRAscope Data

by S. E. Hough and D. S. Dreger

Abstract Source parameters of the *M* 6.1 23 April 1992 Joshua Tree mainshock and 86 *M* 1.8 to 4.9 aftershocks are determined using an empirical Green's function methodology. For the aftershocks, deconvolved *P*- and *S*-wave spectra are calculated for 126 pairs of closely spaced events recorded on portable GEOS stations; *S*-wave spectra from the two horizontal components are averaged. The deconvolved spectra are fit by a ratio of omega-square source models, yielding an optimal (least-squares) corner frequency for both the large and the small event in each pair. We find no resolved difference between the inferred *P*- and *S*-wave corner frequencies. Using the standard Brune model for stress drop, we also find no resolved nonconstant scaling of stress drop with moment, although we also conclude that detailed scaling systematics would be difficult to resolve. In particular, a weak increase of stress drop with moment over a limited moment/magnitude cannot be ruled out. For magnitudes smaller than *M* 3 to 3.5, the inferred stress-drop values will be limited by the maximum observable corner frequency value of 60 Hz. For the mainshock, source-time functions are obtained from mainshock recordings at three TERRAscope stations (PFO, PAS, and GSC) using an *M* 4.3 foreshock as an empirical Green's function. The results indicate a fairly simple, single-pulse source-time function, with clear south-to-north directivity and an inferred rupture radius of 5 to 6 km. The deconvolved source-time functions are inverted to obtain a finite-rupture model that gives a robust estimate of rupture dimension. Early aftershocks are found to lie along the perimeters of regions with high mainshock slip. The inferred mainshock stress-drop value, 56 bars, is within the range determined for the aftershocks. Our derived mainshock source spectra do not show resolvable deviation from the omega-square model.

Introduction

The *M* 6.1 Joshua Tree earthquake on 23 April 1992 occurred just north of the Coachella Valley segment of the San Andreas fault (SAF), within the Little San Bernardino Mountains (Fig. 1a; Hauksson *et al.,* 1993). The earthquake had no surface rupture; a 10- to 12-km south-to-north rupture was inferred from the distribution of the early aftershocks (Fig. 1b). The mainshock was preceded by an *M* 4.3 foreshock that occurred in very close proximity to the mainshock hypocenter (Mori, 1994). The Joshua Tree aftershock sequence was notably energetic, producing one *M* 5 aftershock and 10 events with *M* 4 to 4.9; altogether, over 6,000 aftershocks were located by the Southern California Seismic Network (Hauksson *et al.,* 1993). The sequence was the most productive relative to its mainshock magnitude of any southern California sequence in recent decades (K. Hutton, personal comm., 1992).

The Joshua Tree mainshock was recorded on scale by six broadband TERRAscope stations, which also recorded larger events within the aftershock sequence. Supplementing the permanent station coverage, portable instruments were deployed by both the U.S. Geological Survey (USGS; Hough *et al.,* 1993) and institutions comprising the Southern California Earthquake Center. The USGS instruments consisted of portable digital GEOS recorders (Borcherdt *et al.,* 1985) with Mark Products L-22 2-Hz sensors and Kinemetrics force-balance accelerometers (fbas) at eight sites, with a sampling rate of 200 samples/sec. Most of the stations were deployed specifically to study site effects within sedimentary basins; most of the data used in this investigation will be from one station (FVS; Fig. 1) for which the waveforms were relatively less complex. Between 25 April and 27 June 1992, the GEOS instruments recorded several hundred of the

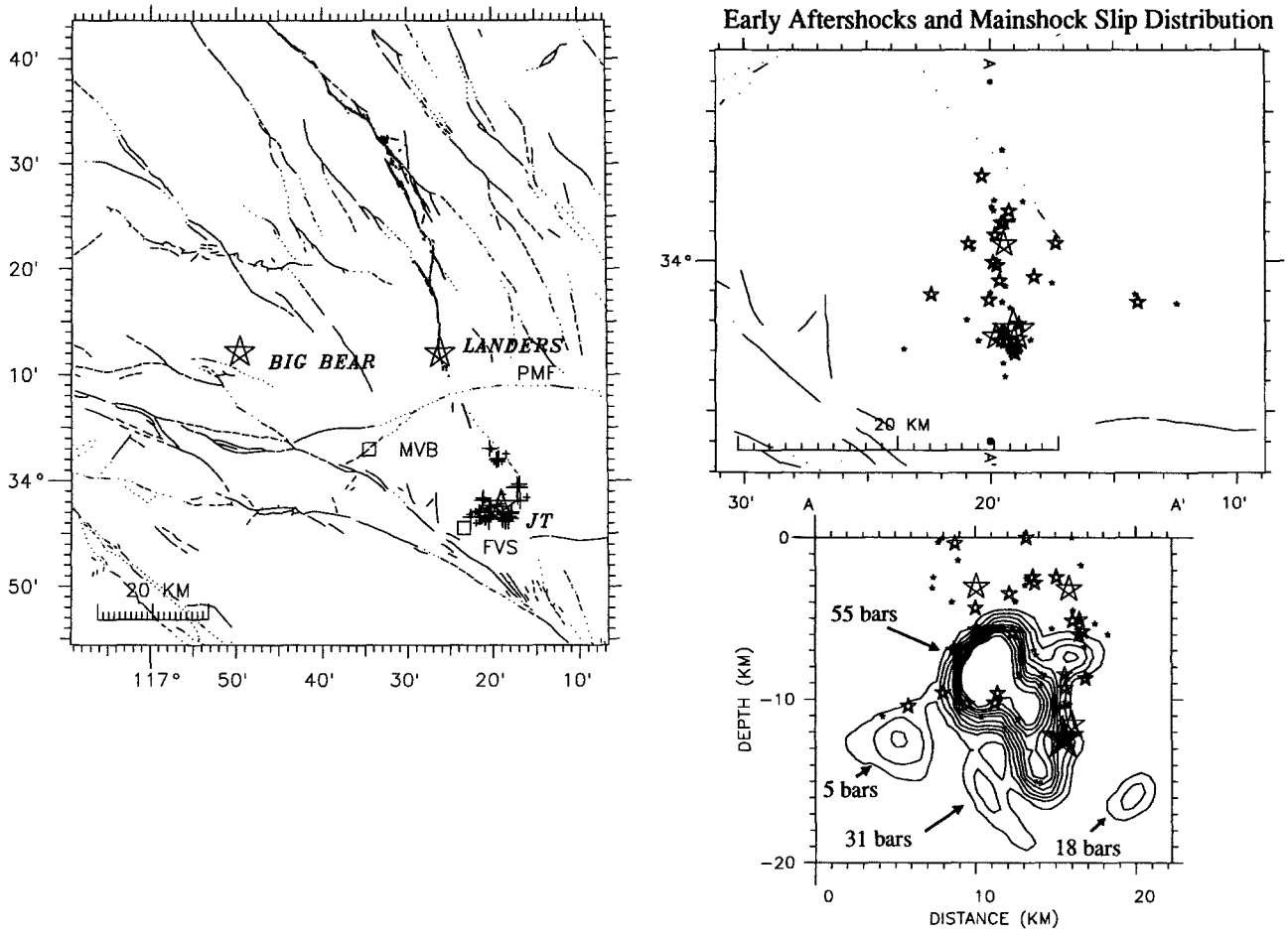

Figure 1. (a) Regional setting of the Joshua Tree earthquake, including the epicenters of the Joshua Tree, Landers, and Big Bear mainshocks. The Landers' surface rupture is indicated by a dark (segmented) line, and the Pinto Mountain fault, which generally delimits the Joshua Tree and Landers sequences, is indicated by "PMF." The locations of events for which stress-drop results are obtained in this study are indicated by crosses (with sizes scaled to magnitude), and the two stations (FVS and MVB) from which data are recorded are indicated by small squares. The empirical Green's function events are not shown if no reliable corner frequency estimate could be made for that event. (b) Joshua Tree region, including the location of the 23 April 1992 *M* 6.1 mainshock (large star) and aftershocks in the first 12 hours (smaller stars, scaled by magnitude). The contours indicate the mainshock slip distribution, as estimated from the finite fault inversion. Contour intervals are 10 cm. Static stress-drop values are estimated for individual patches, assuming an equivalent circular fault area.

(mostly larger) aftershocks. These recordings have been associated with events in the Southern California Seismic Network (SCSN) catalog.

The range of magnitudes and the number of events recorded within the Joshua Tree sequence, including regional broadband recordings of the mainshock itself, make it well suited for investigations into seismic source properties over the range *M* 2 to 6, including investigations into the scaling of stress drop with moment.

The scaling of seismic stress drop remains a relevant issue, one that bears both on theoretical aspects of earthquake source processes (e.g., Dieterich, 1979) and on the prediction of earthquake ground motion for engineering purposes (e.g., Boore, 1983). To further address this issue, it is necessary to obtain stress-drop estimates over a broad range of earthquake magnitudes, from tectonically distinct regions.

As discussed in numerous studies, analysis of small events is complicated by the spectral properties at high frequencies, where path and site effects are not easily distinguished from source effects (Hanks, 1982; Frankel, 1982; Anderson and Hough, 1984; Vernon, 1989). Anderson (1986) presents theoretical results that illustrate how attenuation can yield an apparent corner at frequencies lower than the true corner frequency. Although corner frequencies for small events may not be determined reliably from individual spectra, the comparative study of spectra from a range of

magnitudes using an empirical Green's function technique can permit independent resolution of attenuation and corner frequency (Bakun and Bufe, 1975; Mueller, 1985; Hutchings and Wu, 1989; Frankel *et al.,* 1986; Mori and Frankel, 1990; Frankel and Wennerberg, 1989; Hough and Seeber, 1990). The assumptions of this method are that the distortion due to propagation and attenuation through a heterogeneous medium is linear over the magnitude range considered and that a small event provides an "empirical Green's function" (i.e., with a source-displacement spectrum flat up to approximately half of its corner frequency) that can be used to deconvolve propagation effects from a large event with a similar source-receiver path and focal mechanism. The deconvolutions can be interpreted in either the time domain or the frequency domain.

Frankel and Wennerberg (1989) used the empirical Green's function (eGf) method with data from the Anza network in southern California and showed that there is no evidence for a decrease in stress drop with decreasing source size for moments from $\sim 10^{20.5}$ dyne-cm down to 10^{18} dyne-cm. Abercrombie and Leary (1993) summarize results from numerous high-resolution investigations of stress-drop scaling and show that there is compelling evidence for nonconstant systematic earthquake stress-drop scaling (i.e., increases with moment) over the range 10^{19} to 10^{23} dyne-cm. This result suggests that, on a global scale, earthquake ruptures can be considered self-similar, with no global preferred length scale. One recent study supports this conclusion, presenting evidence from Mexican earthquakes that, if anything, suggests a slight decrease of stress drop with moment for moments up to 10^{28} dyne-cm (Humphrey and Anderson, 1995).

It has been postulated that, within isolated tectonic regimes, preferred length scales might result from structural controls, such as the width of the fault zone (Aki, 1987; Guo *et al.,* 1995). There is also evidence that observed apparent stress, which is proportional to static stress drop, also scales with moment (e.g., Kanamori *et al.,* 1993).

Despite the innumerous observational studies of source properties of small-to-moderate earthquakes, there remains no clear concensus regarding several fundamental issues: (1) Does stress drop vary, randomly and universally, between roughly 1 and 1,000 bars, or (2) is there any systematic behavior in stress-drop variations? Because stress drop fundamentally reflects earthquake rupture size (for a given moment), any nonconstant stress-drop scaling would generally indicate a departure from strict self-similarity of earthquake rupture processes. Any such departure would, in turn, provide an important constraint for physical models of earthquake rupture.

In this study, we present frequency- and time-domain results from application of the eGf method to a recently collected, substantial data set: broadband TERRAscope mainshock data and aftershock data from weak- and strong-motion portable digital instruments. We will obtain source parameters for earthquakes spanning the magnitude range of 1.8 to 6.1 and examine the implications of these results for the scaling issues discussed earlier. In particular, we will address the inherent limitations in resolution for any analysis of this type, to focus on the following question: To what extent can we expect to obtain observational constraints on earthquake source scaling at small magnitudes? We will also discuss our results in the context of previous results on apparent and static stress estimates.

Empirical Green's Function Analysis

Mainshock

Figure 2a presents waveforms of the Joshua Tree mainshock and the M 4.3 23 April 1992 foreshock, recorded on three broadband TERRAscope stations. To obtain source-time functions, a spectral deconvolution method using a water level correction of 1% to 5% of the maximum spectral level (1% for stations GSC and PAS; 5% for PFO) was applied to the respective records shown in Figure 2a. Both the eGf and the mainshock records are rotated to obtain a tangential component, integrated to displacement, and bandpass filtered between 0.02 and 5 Hz using a 2-pole Butterworth filter prior to the deconvolution.

The S-wave deconvolutions are found to be stable, yielding simple, single-pulse source-time functions at the three stations (Fig. 2b). The corresponding source spectra are shown in Figure 3 and will be discussed in a later section. The narrow pulse width at GSC to the north and broader pulse at PFO to the south is indicative of south-to-north directivity. This is consistent with the distribution of early aftershocks. A similar south-to-north directivity was inferred for the foreshock by Mori and Jones (1992); to the extent that this event has its own directivity, the directivity inferred for the mainshock could be an underestimate. However, Mori (1994) shows that the foreshock duration is quite short, 0.1 to 0.2 sec, compared with our inferred mainshock durations; our mainshock source-time functions are thus considered to be representative of the actual source duration.

Assuming that the mainshock source pulses can be approximated by a summation of pulses from spatially distributed subfaults (on the mainshock plane), it is possible to invert the mainshock source pulses for the slip distribution. In this manner, the timing of the individual subfaults are controlled by the passage of a radially expanding rupture front, propagating outward at a constant velocity, and the relative station-subfault difference. The relationship between the far-field source-time function, stf_i, and the subfault rupture is linear, given by

$$stf_i(t) = \sum_j^N \frac{\mu A u_j}{M_0} B_{ij}(t - \tau_{ij}), \qquad (1)$$

where A is the subfault area, μ is the rigidity, M_0 is the total seismic moment (obtained independently), B_{ij} is the source-time function generated by each subfault, and u_j is the slip at the jth subfault. The indices i and j refer to the station and

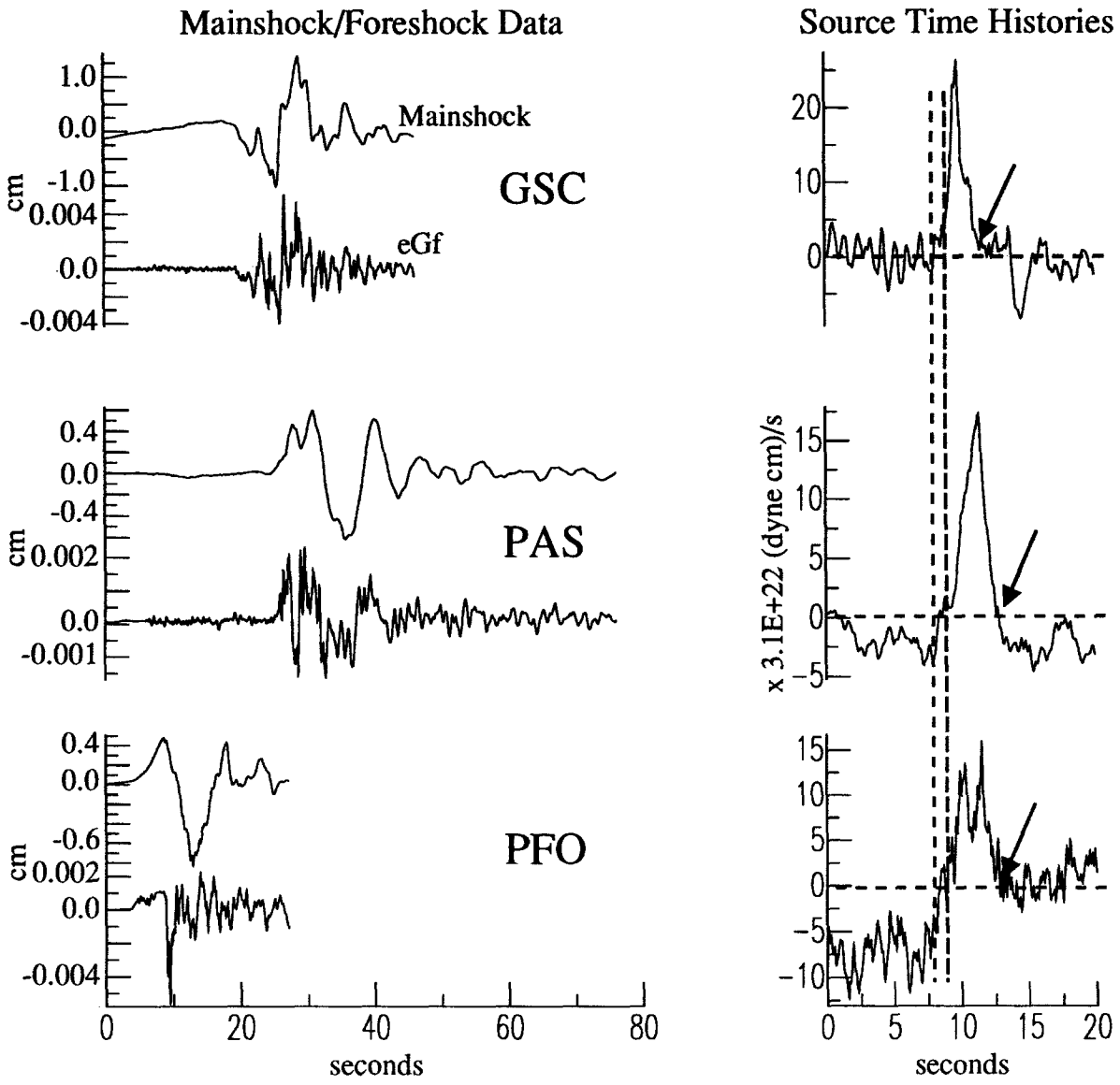

Figure 2. (a) Broadband displacement recordings of the Joshua Tree mainshock at stations GSC (top), PAS (middle), and PFO (bottom). For each station, the mainshock record is the upper trace and the foreshock record is the lower trace. The mainshock seismograms for GSC and PFO were obtained by doubly integrating FBA-23 accelerograms. The mainshock record for PAS and all of the foreshock records were obtained by integrating the STS-1 velocity data. (b) Source-time functions obtained by deconvolving the event pairs shown in (a). The dashed lines indicate the inferred source-time function beginning chosen based on two different criteria, discussed in the text. The arrows indicate the inferred end of the source-time functions.

subfault, respectively. The delay τ_{ij} depends on both the receiver-subfault distance and the assumed rupture velocity. In matrix form, equation (1) becomes

$$\begin{pmatrix} B \\ d/dA \end{pmatrix} w = \begin{pmatrix} d \\ 0 \end{pmatrix}, \tag{2}$$

where d/dA is a spatial differential operator that is minimized and w is slip weight equal to $(\mu A u_j)/M_0$. This system of equations is solved using a nonnegative least-squares approach, with a smoothness constraint imposed by the differentiation operator (Lawson and Hanson, 1974). A detailed discussion of the method is presented by Mori and Hartzel (1990), Mori (1993), and, as applied to regional distance data, Dreger (1994).

We use a vertical plane striking N20°W consistent with the distribution of aftershocks (Fig. 1) and the first-motion focal mechanism of Hauksson *et al.* (1993). The allowable dimension of the fault was 30 km along strike and 20 km in depth, with 1-km-square subfaults. Only about one-third (170) of the possible 600 subfaults resulted in nonzero so-

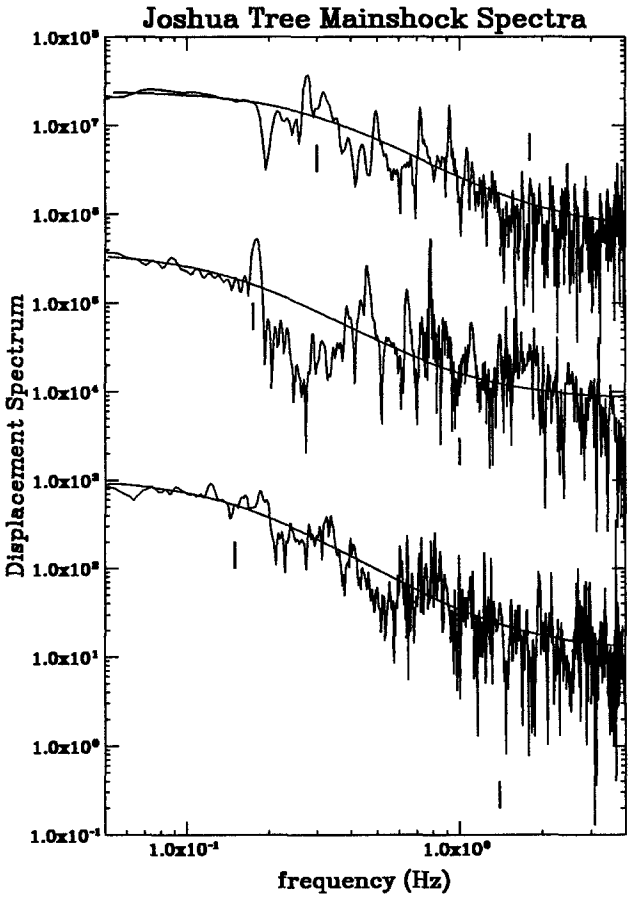

Figure 3. Source spectra corresponding to the source-time functions shown in Figure 2(b). Tick marks indicate inferred corner frequencies.

lutions, yielding a relatively compact slip distribution that maps north of the hypocenter (Fig. 1). Peak slip is on the order of 200 cm, and the average slip is 32 cm. The average slip in the principle slip patch is 58 cm. The rupture velocity found to best satisfy the data was 3 km/sec (82% of the shear-wave velocity used), a similar value to that obtained by Mori (1994) for the foreshock. The long dimension from the hypocenter to the outside edge of slip is approximately 10 km. Although the slip map is relatively simple, there are outliers of relatively low-amplitude slip.

It is interesting to note that the early aftershocks cluster around the localized region of high slip. Mendoza and Hartzell (1988) found that for a suite of large earthquakes, there was a negative correlation between the locations of early aftershocks and regions on the fault that experienced the greatest slip, suggesting a net stress increase in adjacent regions. The slip patches located outside the main patch are not well resolved and are the result of the inversion attempting to model source-pulse complexity at PFO, which is the noisiest of the deconvolutions. The average slip along the primary mainshock rupture is found to be 58 cm. We will discuss the implications of these results for mainshock stress drop in a later section.

Aftershocks

To identify pairs of events for empirical Green's function analysis, we search the SCSN catalog of associated events for pairs that have epicentral distances within 1 km and magnitude differences of at least 0.7 units. These criteria are similar to what has been used in other studies (e.g., Xie *et al.*, 1991; Guo *et al.*, 1995) and provide a preliminary identification of suitable pairs.

With each candidate pair, we estimate deconvolved source spectra. We use pairs of L22 recordings where possible so that the eGf method will deconvolve out a common instrument response. This removes any possible uncertainty associated with variations in response. Menke *et al.* (1991) have documented variability in the actual corner frequency of the L22 instruments, as well as spurious resonances at frequencies about 20 to 25 Hz. For the 10 largest aftershocks, it is necessary to use fba recordings because the weak motion recordings are clipped. We have compared results in a number of cases in which it is possible to use both recordings for the larger aftershock and have not observed any significant differences. However, uncertainty in instrument response may provide an additional source of possible error for these cases.

Time windows including 1 to 3 sec and 3 to 5 sec of the *P*- and *S*-wave arrivals, respectively, are used. Results were more stable, especially at the longer periods, for windows several seconds long instead of windows that include only the initial arrivals. (Although longer windows potentially introduce contamination from scattered energy, the spectra are dominated by direct-wave energy). Shorter windows were necessary for waveforms with either very short *S-P* times or *P* waves that clip sometime after the initial arrival. The time series are tapered with a 5% cosine taper at each end, and spectra are computed using a standard FFT. The spectra are smoothed with a running average prior to computation of the spectral ratio. In the recordings analyzed, signal was above noise up to frequencies of at least 30 Hz; in many cases, it was up to 60 to 70 Hz.

A deconvolved source spectrum is obtained at each station that recorded each pair of events. These source spectra should be independent of site and path effects and should exhibit the same characteristics, except for a directivity effect on corner frequency (e.g., Frankel *et al.*, 1986). Of the 207 event pairs, 122 are found to yield deconvolved source spectra that are judged to be stable. If a given event pair satisfies the assumptions of the eGf method, the deconvolved source spectra will be well modeled by a theoretical ratio of source spectra. For illustration, Figure 4 presents nine averaged (N–S and E–W) horizontal deconvolved source spectra. These examples are not selected by any quality criteria: they are from the first nine pairs (of a somewhat arbitrary list of potential eGf pairs) for which a stable average source spectrum is obtained. As Figure 4 illustrates, the fits are not always perfect. In some cases, a fall-off higher than ω-squared is suggested, such as the upper left example. In some

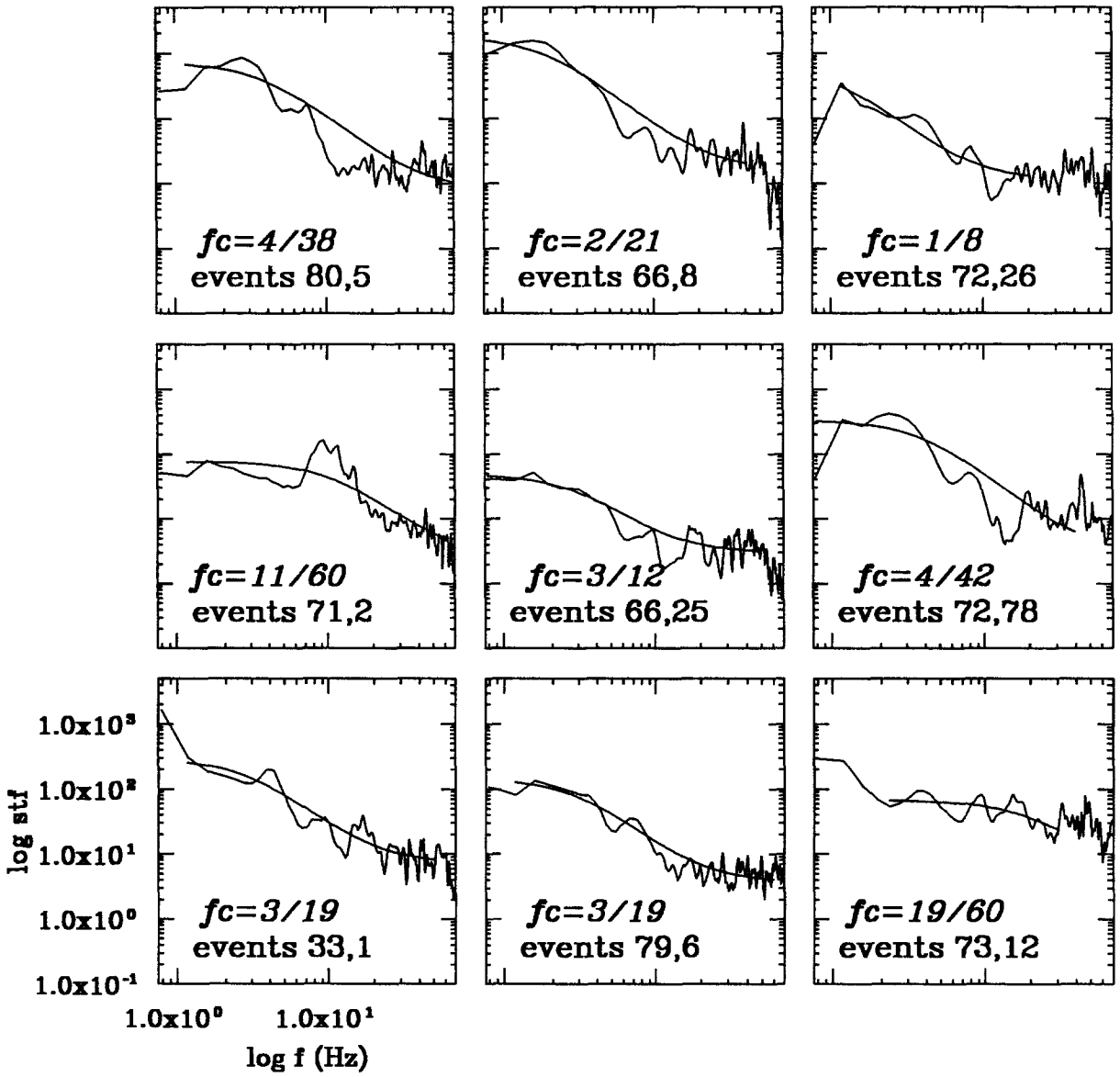

Figure 4. Averaged horizontal deconvolved source spectra from empirical Green's function analysis of nine (arbitrarily chosen) event pairs. Superimposed line indicates best-fitting ratio of omega-square spectra; the optimal corner frequency pair (large event/small event) is given in each panel. Event numbers (large, small) are given for each pair. Corner frequencies do not necessarily match the average values given in Table 1; the values shown here are for the individual source spectrum only.

cases, such as the upper right example, one could conjecture that the inferred upper corner frequency is higher than the true corner, with the true corner frequency outside the frequency band of the data. The decision to use or discard a given deconvolved source spectrum is thus subjective; we will discuss possible biases and resulting uncertainties in a later section.

Each of the final 122 deconvolved source spectra is modeled by a ratio of omega-square source spectra between lower and upper frequency limits of 0.5 to 3 Hz and 20 to 70 Hz, respectively. The range is determined independently for each deconvolved source spectra, based on a subjective assessment of the frequency band over which the results appear stable. Using a parameter search method, corner frequencies are fit in each case so as to minimize the least-squares residuals to the observed spectra. Each individual spectrum is thus assumed to be modeled by

$$A(f) = \frac{A_0}{f^2 + f_c^2}. \tag{3}$$

We solve for the two corner frequencies, f_{c1} and f_{c2}, by min-

imizing the least-squares residual between the computed spectral ratio $R_c(f)$ and the modeled ratio $R_m(f)$:

$$R_m(f) = \frac{A_{01}[1 + (f/f_{c2})^2]}{A_{02}[1 + (f/f_{c1})^2]}. \quad (4)$$

A grid-search method is used to determine the optimal pair of corner frequencies. For each pair of corner frequencies, we perform a regression to find the optimal least-squares amplitude ratio; we choose the corner frequency pair that yields the lowest overall misfit to the data.

Uncertainties Associated with f_c Estimates

To estimate the reliability of corner frequency estimates for the events shown in Figure 4, we calculate the root mean square misfit between the modeled and observed ratio of spectra for a grid of corner frequency pairs (Guo *et al.*, 1994). Figure 5 presents an example of the contoured misfit values for a single deconvolved spectral ratio (between event numbers 1 and 4). This example is typical in that the uncertainty associated with the corner frequency of the larger event, f_{c1}, is smaller than that associated with the smaller corner frequency event, f_{c2}. It also suggests that a minor trade-off exists between the two corner frequencies.

An assessment of error bars from the calculations illustrated in Figure 5 can be made only if one makes a subjective determination of the maximum acceptable misfit increase above the optimal value. Assuming that a misfit within 20% of the optimal is acceptable, Figure 5 implies a corner frequency range of roughly 4 to 12.5 Hz, which in turn implies a stress-drop uncertainty of a factor of 30.

Alternatively, the uncertainty associated with the corner frequency estimates can be evaluated by considering the consistency of results for the same event using different eGfs. Table 1 presents the final *S*-wave results, including an estimate of the standard deviation for those events for which corner frequency is determined from more than one eGf pair. Although this estimate of uncertainty is still not ideal, it is felt to give the most representative illustration of the resolution of the corner frequency estimates.

For the five events greater than M 4 ($M_0 > 10^{22}$ dyne-cm), we obtain standard deviations of 0.27 to 1, corresponding to average corner frequencies of 2.3 to 4 Hz. The corner frequencies obtained for these larger events appear to be more consistent than the corner frequencies for the smaller-magnitude events. We will discuss possible remaining biases in these estimates in a later section.

Stress-Drop Estimation

Stress drop, σ, can be estimated assuming a circular rupture either from the corner frequency, using

$$\sigma = M_0 \left[\frac{f_c}{0.49\beta}\right]^3, \quad (5)$$

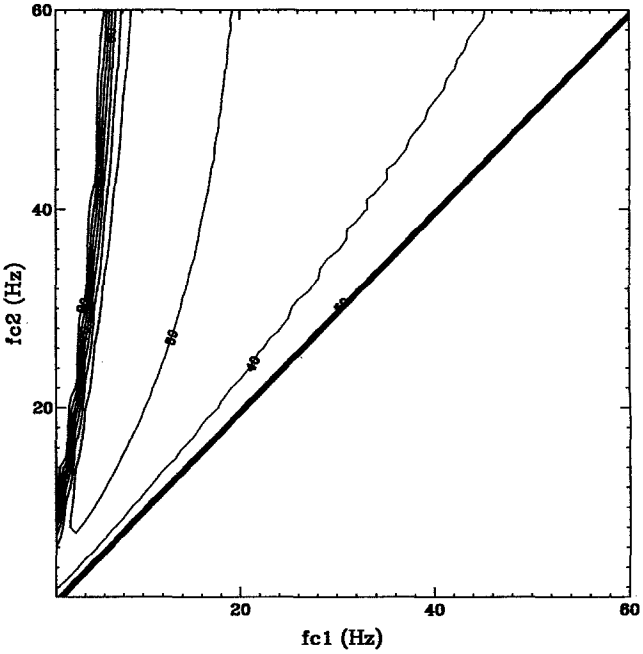

Figure 5. Contoured misfit values for trial corner frequency pairs for the deconvolved spectral ratio between event numbers 1 and 4.

where the velocity term β is the shear-wave velocity near the source, or from the pulse width, using

$$\sigma = \frac{7}{16}\frac{M_0}{r^3}, \quad (6)$$

where r is the source radius (Eshelby, 1957). Equation (6) is derived from equation (5), assuming that $f_c = 0.37/\tau_{1/2}$, a relationship consistent with theoretical dislocation models (e.g., Brune *et al.*, 1979). However, modeling results yield an appreciable scatter in the coefficient of proportionality, which will be influenced by directivity.

Moment, M_0, of the mainshock is determined to be 1.9×10^{25} (Kanamori *et al.*, 1993). For the aftershocks, M_0 values are determined from the body-wave magnitudes using the scaling relationships

$$\log(M_0) = 1.5m_l + 16 \quad (7)$$

and

$$\log(M_0) = 1.1m_l + 17 \quad (8)$$

for $m_l > 3.0$ and $m_l < 3.0$, respectively (these two expressions are equivalent for $m_l = 2.5$; we use M 3 based on the ranges for which the relations were determined). These equations were developed for California earthquakes by Bakun (1984). Equation (8) is motivated by the combined results of Bakun (1984) and Hanks and Boore (1984); Hanks and Boore (1984) show that a scaling break below magnitude 3

Table 1.
S- and P-wave results

N	s/l	dayhrmn	lat	long	log(M_o)	f_{cs}	δf_{cs}	σ_s	f_{cp}	δf_{cp}	σ_p
1	l	1162237	33.9590	-116.3288	19.31	22.5	3.5	41.0	60.0		777.3
2	s	1162335	33.9553	-116.3553	19.64	60.0		1661.7	60.0		1661.7
3	s	1170103	33.9637	-116.3180	19.53	9.0		4.4	60.0		1289.9
4	l	1170117	33.9598	-116.3242	20.08	7.0		7.3			
5	s	1170220	33.9547	-116.3413	19.75	38.0		543.8	60.0		2140.7
6	s	1170225	33.9557	-116.3555	19.31	19.0		24.7	35.0		154.3
7	s	1170251	33.9908	-116.2847	19.75	9.0	2.0	7.2	13.0	2.0	21.8
8	s	1170327	33.9397	-116.3442	18.87	21.0		12.1	29.0		31.9
9	s	1170349	33.9448	-116.3130	19.20	37.0	6.0	141.7	9.0	6.0	2.0
10	s	1170432	33.9512	-116.3678	19.31	9.0		2.6	17.0		17.7
11	s	1170510	33.9565	-116.3462	19.42	12.0		8.0	13.0		10.2
12	s	1170600	33.9467	-116.3082	19.20	60.0	0.0	603.3			
13	s	1170610	33.9502	-116.3628	19.31	6.0		0.8	39.0		213.5
14	l	1170720	33.9745	-116.2683	19.75	8.0		5.1			
15	s	1170949	33.9688	-116.2803	21.10	21.0		2056.5	13.0		3.7
16	l	1170955	33.9428	-116.3593	21.40	1.5	0.3	1.5	8.5	1.7	271.9
17	s	1171149	34.0300	-116.3297	19.53	11.0		7.9	60.0		1289.9
18	s	1171552	33.9695	-116.3487	19.31	44.0	15.0	306.5	28.0	13.0	79.0
19	s	1171609	33.9700	-116.3530	19.53	60.0		1290.0	12.0		10.3
20	s	1181818	33.9417	-116.3648	18.98	7.0	2.1	0.6	60.0	0.0	363.5
21	s	1181026	33.9372	-116.3552	19.53	8.0		3.1	12.0		10.3
22	s	1182056	33.9553	-116.3452	19.53	23.0		72.6	5.0		0.7
23	s	1190030	33.9418	-116.3080	19.64	7.5	2.5	3.2	5.0	0.0	1.0
24	s	1190243	33.9420	-116.3102	19.42	18.3	0.9	28.4	9.0	3.0	3.4
25	s	1190318	33.9448	-116.3435	19.97	20.3	7.4	137.6	13.3	4.4	38.7
26	s	1190732	33.9388	-116.3093	20.30	5.0		4.4	8.0		18.0
27	s	1190959	33.9375	-116.3472	19.53	22.0		63.6	12.0		10.3
28	s	1191040	33.9465	-116.3000	19.09	23.3	2.5	27.4	22.5	3.5	24.7
29	s	1191113	33.9402	-116.3010	20.19	5.0	1.0	3.4	3.0		0.7
30	l	1191151	33.9452	-116.3073	19.42	17.0		22.8	8.0		2.4
31	l	1191427	33.9492	-116.2967	19.97	4.0		1.1	4.0		1.1
32	s	1191432	33.9483	-116.2983	20.30	6.0	0.0	7.7	7.5	0.6	14.8
33	l	1191525	33.9598	-116.3250	21.10	3.0	0.6	6.0	20.5	0.5	1911.5
34	s	1201310	33.9438	-116.3025	20.30	4.6	1.0	3.4	7.4	2.1	14.2
35	s	1201945	33.9370	-116.3763	18.87	22.0		13.9	44.0		111.3
36	l	1211043	33.9687	-116.2857	19.86	3.0		0.3	4.0		0.8
37	s	1211058	33.9660	-116.3538	18.65	34.0	8.0	30.9	25.5	1.5	13.1
38	s	1211240	33.9357	-116.3477	19.20	60.0		603.3	34.0		109.8
39	s	1211332	33.9462	-116.3158	20.65	14.0		216.0			
40	l	1211555	33.9332	-116.3657	20.19	5.5	3.5	4.5	43.0	5.0	2170.3
41	s	1211658	33.9428	-116.3595	19.42	10.0	1.0	4.6	16.0		19.0
42	l	1220603	34.0352	-116.3213	21.10	6.0		47.9	7.0		76.1
43	s	1220800	34.9546	-116.3565	19.75	48.0	4.0	1095.4	46.5	6.5	61.4
44	l	1220819	33.9787	-116.3147	20.19	6.0		5.9	18.0		159.2
45	s	1221215	33.9500	-116.3152	19.20	33.0	9.0	100.4	32.0	21.0	91.5

(*continued*)

results from the transition to corner frequencies that are above the frequency response of the Wood–Anderson instrument. We do not determine M_0 directly from long-period spectral levels because of the sensitivity of this type of estimate to the radiation term, the half-space assumption, and the poor azimuthal coverage of our stations (i.e., general systematics in event mechanism could alias into systematic biases in moment estimation).

In many cases, we obtain multiple corner frequency estimates for individual aftershocks, usually from deconvolutions with more than one event. Each deconvolved spectra is fit individually; multiple corner frequency estimates are then averaged to give one *P*- and *S*-wave corner frequency for each event, a total of 74 and 86 events, respectively (Fig. 6).

Figure 6 also includes results for the magnitude 4.3 foreshock; a range of estimates is shown, as determined via a finite-fault inversion by Mori (1994). The range for this event is high (320 to 870 bars) but consistent with the results obtained for the larger of the aftershocks. From the regressions shown in Figure 3b, we obtain an average corner frequency of ≈1.4 Hz, corresponding to a much lower stress-drop value, 14 bars. However, we consider this estimate to be considerably less well resolved than that of Mori (1994). For illustration, we consider the mainshock deconvolved source spectrum at PAS (Fig. 3): If the foreshock corner frequency is constrained to be consistent with Mori's (1994) stress-drop estimate (that is, 4.9 Hz), we obtain a mainshock corner frequency of 0.2 Hz, instead of 0.15 Hz, with an imperceptible difference in the quality of the spectral fit. This mainshock corner frequency value is closer to that which would be predicted from the pulse width at this station, using $0.37/\tau_{1/2}$.

The mainshock stress drop can be estimated both from the finite-fault model and from our inferred source-time functions. We first examine the implications of our inferred pulse widths; although we will argue that the finite-fault results are more robust, this consideration provides useful in-

Table 1.
Continued

N	s/l	dayhrmn	lat	long	log(M_o)	f_{cs}	δf_{cs}	σ_s	f_{cp}	δf_{cp}	σ_p
46	s	1221338	33.9375	-116.3150	20.19	20.0	19.0	218.4			
47	s	1222059	33.9385	-116.3148	18.98	37.0	8.7	85.3	32.4	10.5	57.2
48	s	1230352	33.9583	-116.3313	19.42	15.5	7.5	17.3			
49	s	1230527	33.9615	-116.3372	19.42	60.0		1001.3			
50	s	1230542	33.9432	-116.3402	18.87	51.3	5.9	176.4	58.3	8.4	258.9
51	s	1230942	33.9545	-116.3412	19.86	60.0		2757.8	28.0		280.3
52	s	1231207	33.9595	-116.3403	19.53	55.5	4.5	1021.0	60.0		1289.9
53	l	1231246	33.9897	-116.2867	22.30	4.0	1.0	225.1	5.0		439.6
54	s	1231307	33.9782	-116.2698	18.98	70.0		577.3			
55	s	1231329	33.9952	-116.2830	20.30	13.0		77.3			
56	l	1231910	33.9915	-116.2862	21.40	4.0		28.3			
57	s	1232025	33.9512	-116.3670	19.31	13.0		7.9	25.5	11.6	59.7
58	s	1232305	33.9482	-116.3082	19.09	22.0	3.3	23.0			
59	s	1232320	33.9427	-116.3025	19.64	22.0	12.0	81.0	33.0	14.0	276.5
60	s	1232322	33.9475	-116.3327	18.98	51.0		223.3	60.0		363.5
61	s	1240037	33.9403	-116.3030	21.10	4.0	0.5	14.2	4.0	0.8	14.2
62	s	1240231	33.9425	-116.3097	19.20	19.6	5.5	21.0	9.0	2.7	2.0
63	s	1240553	33.9350	-116.3743	19.20	24.5	14.5	41.1	60.0	0.0	603.3
64	l	1240813	33.9427	-116.3767	20.30	3.5	0.5	1.5	9.0	7.0	25.6
65	s	1240922	34.0495	-116.3355	19.53	60.0		1289.9	58.0		1165.2
66	l	1250116	33.9395	-116.3407	22.15	3.3	0.3	89.5	2.3	0.3	30.3
67	s	1250125	33.9432	-116.3347	19.20	28.0	7.4	61.3	30.0	15.0	75.4
68	s	1250421	33.9810	-116.3173	19.09	60.0		468.3	80.0		1110.1
69	s	1250618	33.9595	-116.3350	19.09	37.0	23.0	109.8	54.0		341.4
70	s	1250833	33.9470	-116.3338	18.65	60.0	0.0	170.0	21.5	8.5	7.8
71	s	1251232	33.9472	-116.3525	18.32	39.5	20.5	22.7	90.0		268.4
72	l	1251619	33.9417	-116.3042	23.35	2.7	0.3	776.7	2.1	0.3	365.4
73	l	1270238	33.9430	-116.3145	23.05	3.6	0.4	922.6	1.7	0.3	97.2
74	s	1270510	33.9405	-116.3152	21.10	8.5	3.5	136.5	10.0	1.0	221.9
75	s	1271741	33.9467	-116.3147	21.40	5.6	1.3	77.7	1.4	0.4	1.2
76	l	1281224	33.9690	-116.3538	20.80	8.5	2.5	68.3	7.0	0.6	38.1
78	s	1290721	33.9465	-116.3148	20.08	13.4	4.2	51.0	31.6	8.1	668.6
79	l	1390022	33.9503	-116.3600	21.40	3.4	0.2	17.4	3.0	0.6	12.0
80	l	1391544	33.9513	-116.3378	23.35	2.3	0.3	480.0	2.4	0.3	545.4
81	l	1392350	33.9610	-116.3398	20.80	9.5	2.0	95.3	11.0	4.0	148.0
82	s	1401215	33.9448	-116.3415	20.65	9.6	3.3	69.6	12.3	2.7	146.5
83	l	1441822	33.9727	-116.3527	20.30	15.0	3.0	118.7	8.0	1.0	18.0
84	s	1451531	33.9418	-116.3492	20.30	44.5	15.5	3008.8	10.0		35.2
85	l	1462306	34.0328	-116.3250	20.30	3.0	1.0	1.0	5.5	3.5	5.9

First entry gives assigned event number, second entry indicates whether event was small (s) or large (l) event used in its eGf pair, third entry gives Julian day (1994), hour, and minute of event. Magnitudes (*mag*) are determined from the SCSN. Moments are determined by scaling relation proposed by Hanks and Boore [1984]. f_{cs}, and σ_s are corner frequencies and stress drops determined from S waves; f_{cp} and σ_p are determined from the P waves. δf_{cs} and δf_{cp} are the standard deviations of the corner frequency estimates, for events for which more than one estimate is obtained.

sights into the validity of the simple theoretical relations and the kinds of uncertainties that result from them. From Figure 2b, we can estimate a source-time function width from both the "narrowest" pulses (NP) and between the zero crossings (ZC). The dashed lines and arrows in Figure 2b illustrate these picks. Both sets of durations show the northward thinning, which is consistent with directivity in that direction. Source radius can be estimated from $t_{0.5}\beta$, where $t_{0.5}$ is the half-duration of the pulse width and β is the shear-wave velocity. We can attempt to account for directivity with the modification

$$r = \frac{t_{0.5}\beta}{[1.25 - \cos(\theta)]}, \tag{9}$$

where we assume a rupture velocity 80% of β and θ represents the angle between the strike of the rupture direction and the azimuth to the station.

Table 2 presents σ_1 and σ_2, the stress-drop estimates corresponding to each source-time function with and without the directivity correction, respectively. Results are shown using both the NP and ZC picks. There is considerable range in the measurements, from 0.5 to 208 bars, demonstrating the unreliability of stress drop computed in this manner. Interestingly, the estimates that incorporate a directivity correction are at least variable than those that do not; this may reflect the fact that directivity corrections become quite large when θ is near 0° or 180°, as are stations GSC and PFO. It may also reflect a breakdown in the one-dimensional directivity model; i.e., our finite fault model suggests that vertical directivity is also important.

To investigate the consistency of our mainshock and aftershock analysis, we can also examine the mainshock deconvolved source spectra shown in Figure 3. Following the procedure used to analyze the aftershocks, we fit ratio of omega-square source models to each of the mainshock spectra. This procedure yields optimal mainshock corner frequencies of 0.175, 0.3, and 0.15 for stations PAS, GSC, and PFO, respectively. These values are generally consistent with the respective values of $0.37/\tau_{1/2}$, 0.24, 0.34, and 0.16. Al-

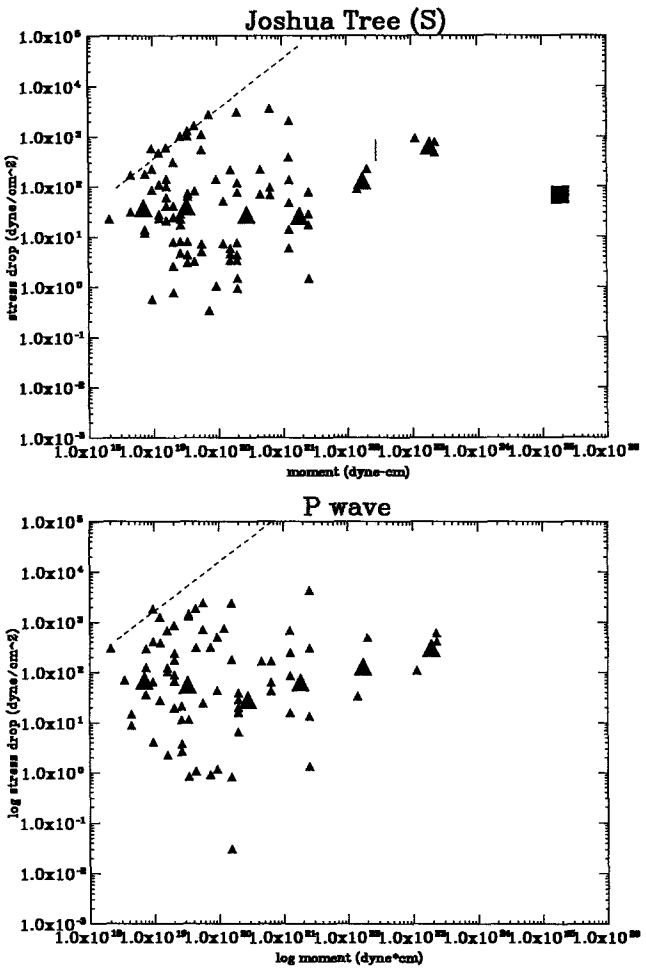

Figure 6. Stress-drop estimates for foreshock, aftershocks, and mainshock. For the aftershocks, stress-drop estimates are made both from (a) the *S* waves and from (b) the *P* waves. A range of values is given for the foreshock, indicated by a solid line; these results are from Mori (1994). Small triangles indicate stress-drop values for each event analyzed (averaged from different empirical Green's function pairs, if more than one was used); large triangles indicate average stress-drop values computed for equal logarithmic moment bins; large square indicates mainshock stress-drop estimate. Dashed line indicates resolution limit imposed by maximum observable corner frequency (see text for discussion): stress-drop values to the left of this line would not be resolvable.

though some degree of complexity is evident in Figure 3b (as is expected given substantial directivity effects), we conclude that, within the resolution limits of the data and the method, no significant departure from an omega-square spectrum is observed for the Joshua Tree mainshock. Stress-drop estimates using the optimal mainshock corner frequencies are thus expected to be consistent with those estimated from the pulse widths (the optimal corner frequencies at stations PAS, GSC, and PFO imply stress-drop values of 18, 90, and 11 bars, respectively, using equation 5).

Table 2.

Stn	θ	NP (s)	ZC (s)	$\sigma_{NP,dir}$	σ_{NP}	$\sigma_{ZC,dir}$	σ_{ZC}
GSC	4	2.0	3.5	2.8	172.4	0.5	32.0
PAS	−61	3.3	4.6	17.2	38.4	6.3	14.2
PFO	−136	3.7	4.9	207.9	27.2	89.5	27.2

Inferred source pulse width parameters for the Joshua Tree mainshock. θ is the angle between the rupture direction and the azimuth to each station. NP and ZC are the "narrow" and zero-crossing pulse width picks, respectively, shown in Figure 2b. σ_{NP} and σ_{ZC} represent stress drop estimates using the NP and ZC pulse widths, respectively; the *dir* subscript indicates values estimated using a directivity correction.

On the other hand, the stress drop may be computed from the slip distribution map directly (Fig. 1). As discussed previously, only the principle slip patch is considered a robust feature. The average slip in this patch is 58 cm and the radius of an equivalent-area circle is 5 km. These values yield a stress drop of 56 bars. If all of the seismic moment is released from a circle with radius 5 km, then a stress drop of 66 bars is obtained. We performed slip inversions using both the NP- and ZC-interpretted source-time functions. The result of this experiment revealed that the average slip and dimension of the principle slip patch do not change, although the small precursory phase in the ZC source-time functions do cause the position of the principle slip patch to translate several kilometers updip and toward the north. (It is possible to estimate stress-drop values corresponding to the secondary slip patches; they are unremarkable, ranging from roughly 4 to 30 bars; Fig. 1). Based on these results, we consider the stress-drop estimates computed from the finite-fault inversion to be a more robust estimate than the values estimated using only pulse widths or corner frequencies. Our preferred value, 56 bars, is shown on Figure 6.

A high level of variability is evident in the aftershock stress-drop values shown in Figure 6. To investigate whether this represents real variability of stress drop or simply high levels of uncertainty, we present in Figure 7 the subset of events for which a standard deviation is estimated from multiple eGf pairs and indicates a variation of less than 30% (see Table 1). These values are somewhat less scattered than those shown in Figure 6, with most values between 1 and 100 bars. However, extreme values are represented within this subset, and the *M* 4 to 5 events persist as notably high stress drop compared with the lower-magnitude events.

Clear differences between very high and very low stress-drop events can be demonstrated via a simple evaluation of waveforms; Figure 8 presents a comparison of two events (event numbers 27 and 84) that have nearly an order of magnitude difference in moment but have a very similar frequency content. The inferred stress-drop values for these events differs by a factor of approximately 50: 64 versus 3,009 bars. These two events are recorded at a short epicentral distance (less than 1-sec *S-P* time; near-field ground motions are evident in event number 84) and have simple

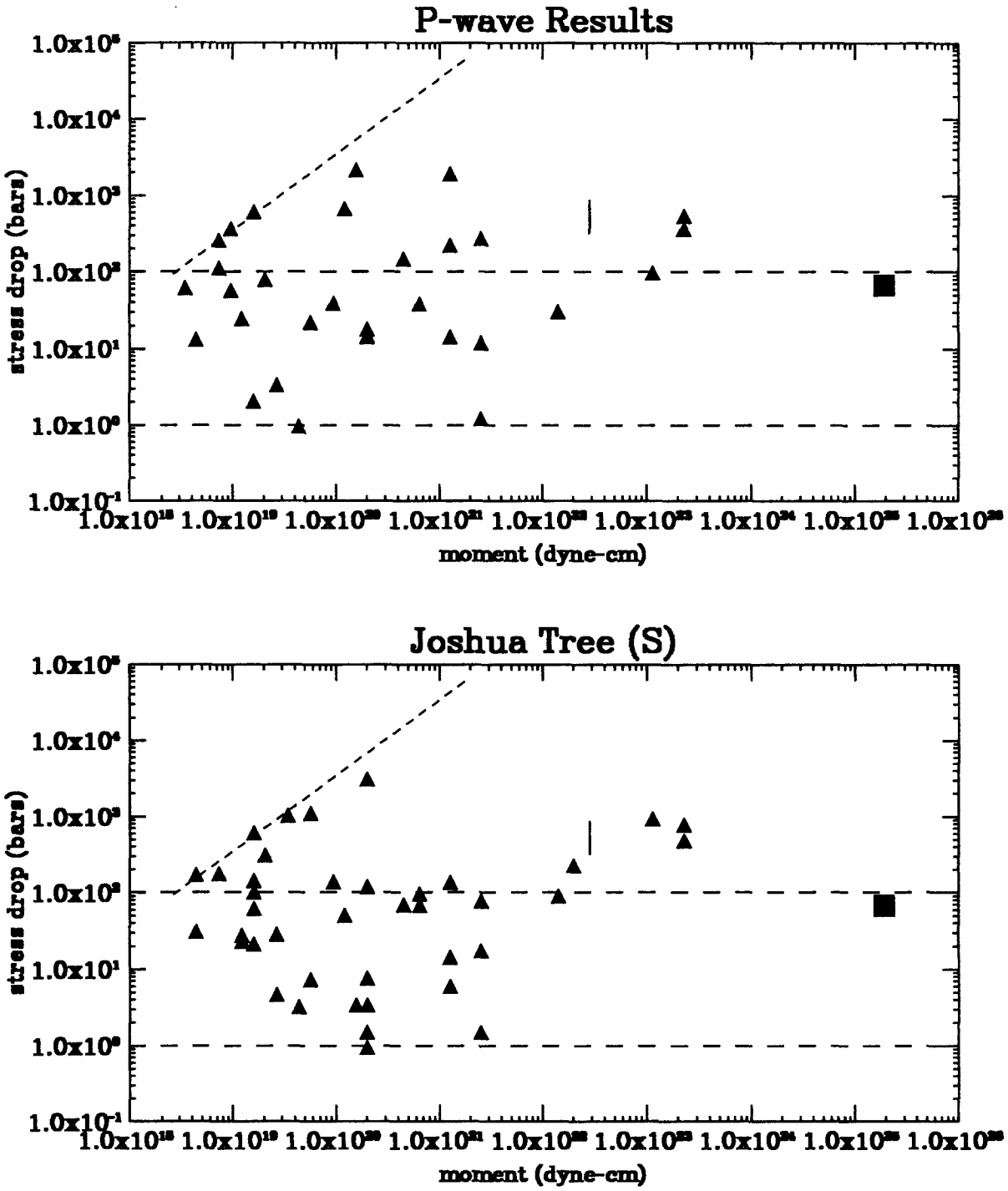

Figure 7. Stress-drop values for those events for which a corner frequency standard deviation (estimated from multiple eGf pairs) indicates a variation of less than 30%. Top figure shows *P*-wave results and bottom shows *S*-wave results. Long dashed lines indicate 1 and 100 bars. Other plotting conventions are consistent with Figure 6.

waveforms, which indicate a relatively uncomplicated propagation path.

In all of the foregoing calculations, one significant source of uncertainty in absolute stress-drop values stems from the particular choice of velocity in equation (5). We use $\beta = 3.64$ km/sec, consistent with the value inferred from our finite-fault inversion. Because this term is cubed in equations (5) and (6), significant changes in stress-drop estimates will result from changes in the assumed value of β. Stress-drop results are therefore much better constrained relative to one another than in absolute value. For the same reason, care is required in the comparison of different published stress-

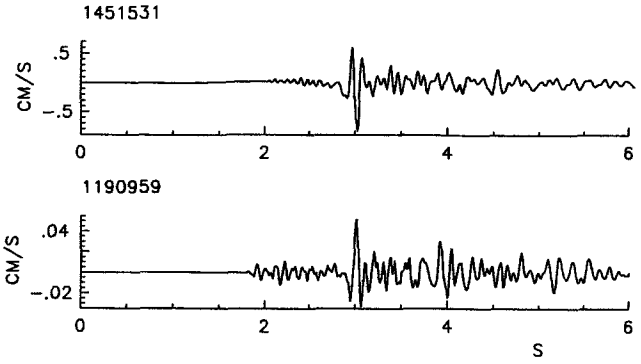

Figure 8. Recorded waveform for event numbers 27 (1190959, bottom) and 84 (1451531, top). These events have amplitudes that differ by approximately a factor of 20 (magnitude 3.0 versus 2.3) but very similar frequency content.

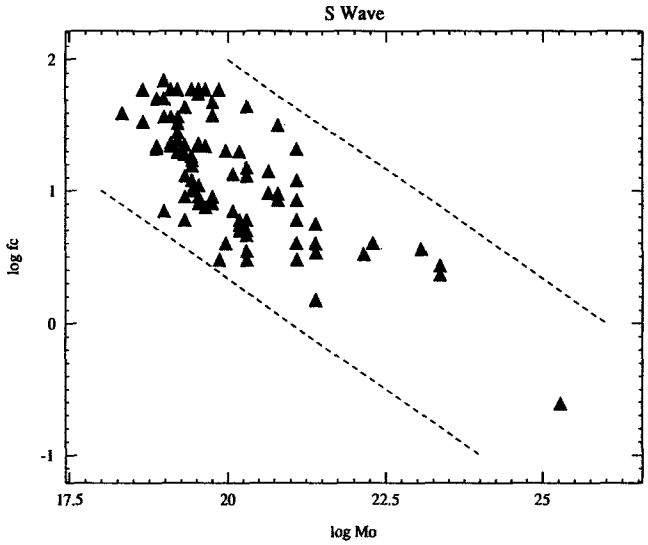

Figure 9. Averaged f_c estimates are plotted against M_0 on a logarithmic scale. The dashed lines indicate constant stress-drop scaling.

drop results. To address the issue of scaling more directly, independent of absolute stress-drop estimates, Figure 9 presents a logarithmic plot of moment versus average corner frequency for the mainshock and aftershocks. For the mainshock, corner frequency is estimated from the pulse width using the relations discussed earlier (equivalently, all of the corner frequencies can be converted to pulse widths).

We do note in Figures 6 and 7 that there is a tendency for the M 4 to 5 events to be characterized by high stress drops. Interestingly, the averaged stress-drop values between 10^{21} and 10^{23} dyne-cm are not inconsistent with the weak scaling inferred in previous studies for apparent stress (e.g., Kanamori *et al.*, 1993; Urbancic and Young, 1993). However, an extrapolation of this relationship to the mainshock moment would imply a mainshock stress drop on the order of 1 kbar. Using equation (5), this, in turn, implies a source radius of approximately 2 km; this is clearly at odds with our results for the Joshua Tree mainshock.

It is also interesting to compare *P*- versus *S*-wave estimates of corner frequency. The relationship between them has been the subject of considerable debate: Many theoretical models suggest a *P*-wave corner frequency greater than that for *S* waves by roughly 1.7 (i.e., the ratio of *P*- to *S*-wave velocities [Molnar *et al.*, 1973]). Other theoretical models predict no difference (e.g., Dahlen, 1974). Using an empirical Green's function method, Xie *et al.* (1991) find a ratio of *P* and *S* corner frequencies of 1.07 ± 0.26 for four aftershocks of the 1983 Goodnow, New York, event. In this study, we obtain a ratio of 1.1 ± 1.7 from the 86 events for which averaged *P*- and *S*-wave corner frequency estimates are determined. For the five largest aftershocks, the corner frequency ratio implied by the difference in average stress drops is 1.3.

Stress-Drop Uncertainties and Comparison with Previous Results

The results of this study can be compared with previously published results for both the mainshock and some of the aftershocks. Both Lindley (1994) and Kanamori *et al.* (1993) obtain a higher-stress-drop value for the mainshock, 203 and 162 bars, respectively (with the latter an apparent stress estimate). These values are within the range we obtain for the mainshock (Table 2). However, they are considerably larger than the value obtained from the slip distribution, which is considered a more robust estimate. In contrast, Lindley (1994) presents a simple corner-frequency estimation for the mainshock, which is not expected to have the resolution of our finite-fault inversion of deconvolved source-time functions. Their average also incorporates more results from more distant TERRAscope stations, which we did not judge to be of suitable quality to use in our deconvolutions. A stress drop of 203 bars implies a rupture radius on the order of 3.5 km, which in turn implies an overall pulse width on the order of 2 sec. This value is smaller than all of our inferred source pulse widths, even for station GSC, at which we expect significant shortening due to directivity effects.

Kanamori *et al.* (1993) obtain an apparent stress estimate that is considerably higher than the static stress estimate obtained in this study; i.e., they obtain a radiated energy value that is high relative to the moment. However, Singh and Ordaz (1994) show that, for an omega-square source model, apparent stress is expected to be $0.43\sigma_b$. Hough and Dreger (1994) extend this result, showing that apparent stress is predicted to be lower than the Brune stress drop for any plausible one-corner source spectral model. It can be shown that apparent stress drop can be higher than predicted for an omega-square model if the source spectrum has an intermediate high-frequency decay over part of its bandwidth (K. Mayeda, personal comm., 1995). Because we have shown that the Joshua Tree mainshock source spectrum is well characterized by an omega-square spectrum, we spec-

ulate that the apparent high radiated energy value estimated by Kanamori *et al.* (1993) may be biased, possibly by inclusion of nondirect phases.

Our aftershock stress drops, on the other hand, are higher than those obtained by Lindley (1994). However, Lindley obtains aftershock stress-drop values from corner frequency estimations from deconvolutions between the mainshock and the aftershocks, rather than between pairs of aftershocks as done in this study. Lindley uses the same methodology as is used in this study, using a large aftershock as the empirical Green's function rather than the large event in the deconvolution, and we have shown in Figure 5 that the corner frequency of the eGf is often poorly resolved. Using the TERRAscope data, the aftershock corner frequencies are approaching the upper limit of usable data in the same way as are the smaller of the events in each eGf pair considered in this study. Thus, all of the aftershock stress drops reported by Lindley (1994) are likely characterized by the similar limited resolution as we infer for our smaller events.

The aftershock stress-drop estimates obtained by Lindley (1994) are possibly biased by the (relatively) low-frequency nature of the TERRAscope data. It is also possible that the larger-aftershock stress-drop estimates obtained in this study are biased by the high-frequency nature of the GEOS data (that is, to the extent that we have misidentified low-frequency corners near or below the bandwidth of our data). However, we have used fba data for the larger aftershocks, which should provide reliable signal to frequencies at least as low as 1 Hz for M 4 to 5 events. We have also tested our regressions using synthetic omega-square spectra with superimposed noise; these tests reveal that corners as low as 0.5 to 1 Hz should be resolvable using our approach.

We have shown that inherent stress-drop uncertainties can easily reach an order of magnitude or more, even when the corner frequency is well within the instrumental bandwidth. Focussing on the results we consider relatively reliable (Fig. 7), we find that stress-drop values tend to cluster within the range 1 to 100 bars, consistent with both high-resolution local studies (e.g., Mori and Frankel, 1990) and teleseismic studies (e.g., Singh and Ordaz, 1994). However, we do find evidence for well-resolved high-stress-drop events, particularly in the magnitude range M 4 to 5.

Discussion and Conclusions

We have shown that an empirical Green's function technique allows independent determination of source properties of earthquakes with magnitudes ranging from 1.8 to 6.1, using data recorded by both the TERRAscope network and by portable instruments deployed following the mainshock. Within the limits of resolution, corner frequency continues to increase with decreasing source size down to a magnitude of 1.8, or a moment of roughly $10^{19.5}$ dyne-cm, consistent with results obtained in other high-resolution studies of source parameters. The stress drop of the mainshock is consistent with the range inferred for the aftershocks.

Variation of corner frequencies for similar-sized events within the Joshua Tree sequence suggests a large variation in stress drop. One fundamental conclusion of this study is that the resolution of source parameters for small events (less than magnitude 3.5 to 4) is found to be fairly limited, even using the empirical Green's function method. Resolution of source properties of even moderate (M 4 to 5) events may also be inherently difficult because typical corner frequencies of this size event often fall near the edge of the instrumental bandwidth. Although we conclude that stress-drop estimates for the M 4 to 5 events presented in this study are relatively reliable, the full uncertainties are difficult to quantify with precision; order-of-magnitude uncertainties appear entirely plausible. For large events, it may be necessary to take into account multi-dimensional source directivity to obtain a reasonable estimate of rupture area and, consequently, static stress drop. We do conclude that it is possible to resolve differences between especially high and especially low stress-drop results; the mere existence of these examples argues for a real variability in stress drop. However, this and other studies (e.g., Humphrey and Anderson) have consistently shown that stress-drop estimates are not systematically different between small-to-moderate and large events. The results from this study thus do provide additional evidence that, for the purposes of extrapolation from moderate-to-large magnitudes, the assumption of constant scaling is justified.

In light of the noted limitations, the issue of stress-drop scaling of small-to-moderate events, which bears critically on an understanding of earthquake source processes, remains elusive. A weak scaling of stress drop with moment over a finite range cannot be ruled out by the observations; this scaling is in fact consistent with previous apparent stress-drop scaling results. However, previous apparent stress results, based on estimates of radiated seismic energy, predict nonconstant scaling over the entire magnitude range (Fig. 10 presents the results of Kanamori *et al.,* 1993, replotted to show energy versus moment), which is not consistent with results of our study. Alternatively, our results could simply indicate a tendency for M 4 to 5 events to be characterized by high stress drops.

We are left with a couple of critical uncertainties regarding the issue of stress-drop scaling: (1) the apparent systematic behavior of apparent stress shown in Figure 10, given the observation evidence (Abercrombie and Leary, 1993; this study) that no strong scaling exists over the entire magnitude range for static stress drop; and (2) the detailed scaling of small-to-moderate events, which bears critically on our understanding of the earthquake rupture processes. Given the paucity of available surface recordings with good signal-to-noise levels at frequencies exceeding 60 Hz, downhole recordings may offer the best hope of ultimate resolution of the latter issue. Additionally, expanded frequency bandwidth within a single sensor-recorder configuration would greatly improve our ability to resolve stress-drop scaling over a significant range of seismic moment.

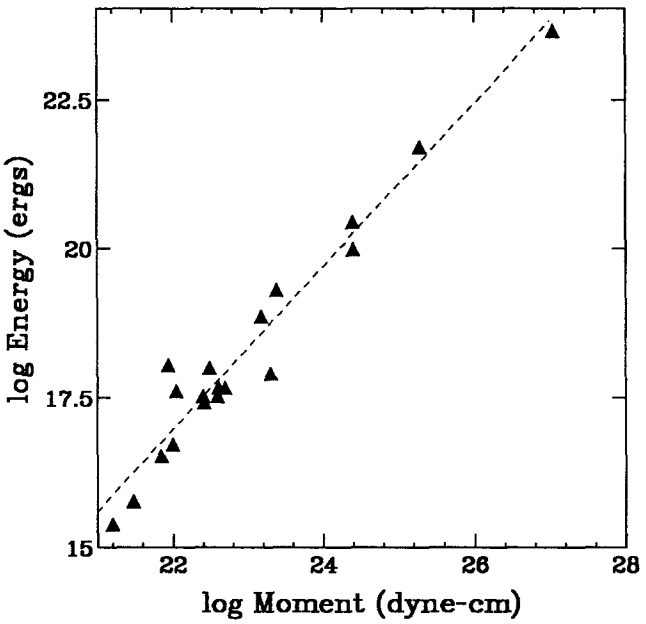

Figure 10. Energy-moment scaling results from TERRAscope recordings of Southern California earthquakes from Kanamori *et al.* (1993), replotted to show implied scaling directly (see Kanamori *et al.*, for details). A slope of 1 would imply constant apparent stress scaling; a regression through the actual results yields a slope of 1.35.

Acknowledgments

The authors acknowledge the many people who participated in the GEOS instrument deployment and preliminary data processing, including Gene Sembera, Jim Mori, Chris Dietel, Leif Wennerberg, and Gary Glassmoyer. We thank Dave Boore and Rachel Abercrombie for helpful discussions and constructive criticisms and an anonymous reviewer for their comments.

References

Abercrombie, R. and P. C. Leary (1993). Source parameters of small earthquakes recorded at 2.5 km depth, Cajon Pass, California: implications for earthquake scaling, *Geophys. Res. Lett.* **20,** 1511–1514.

Aki, K. (1987). Magnitude-frequency relation for small earthquakes: a clue to the origin of f_{max} of large earthquakes, *J. Geophys. Res.* **92,** 1349–1355.

Anderson, J. G. and S. Hough (1984). A model for the shape of the Fourier amplitude spectrum of acceleration at high frequencies, *Bull. Seism. Soc. Am.* **74,** 1969–1994.

Anderson, J. G. (1986). Implication of attenuation for studies of earthquake source, in *Earthquake Source Mechanics,* American Geophysical Monograph 37, 311–318.

Bakun, W. H. and C. G. Bufe (1975). Shear wave attenuation along the San Andreas fault zone in central California, *Bull. Seism. Soc. Am.* **65,** 439–459.

Bakun, W. H. (1984). Seismic moments, local magnitudes, and coda-duration magnitudes for earthquakes in Southern California, *Bull. Seism. Soc. Am.* **74,** 439–458.

Boore, D. M. (1983). Stochastic simulation of high frequency ground motions based on seismological models of the radiated spectra, *Bull. Seism. Soc. Am.* **73,** 1865–1894.

Brune, J. N. (1970). Tectonic stress and the seismic shear waves from earthquakes, *J. Geophys. Res.* **75,** 4997–5009.

Brune, J. N., R. J. Archuleta, and S. Hartzell (1979). Far-field S-wave spectra, corner frequencies, and pulse shapes, *J. Geophys. Res.* **84,** 2262–2272.

Dahlen, A. (1974). On the ratio of *P*-wave to *S*-wave corner frequencies for shallow earthquake sources, *Bull. Seism. Soc. Am.* **64,** 1159–1180.

Dieterich, J. (1979). Modeling of rock friction: 1. Experimental results and constitutive equations, *J. Geophys. Res.* **84,** 2161–2168.

Dreger, D. S. (1994). Empirical Green's function study of the January 17, 1994 Northridge, California earthquake, *Geophys. Res. Lett.* **21,** 2633–2636.

Eshelby, J. D. (1957). The determination of the elastic field of an ellipsoidal inclusion and related problems, *Proc. Roy. Soc. London, Series A* **241,** 376–396.

Frankel, A. (1982). The effects of attenuation and site response of the spectra of microearthquakes in the northeastern Carribean, *Bull. Seism. Soc. Am.* **72,** 1379–1402.

Frankel, A., J. Fletcher, F. Vernon, L. Haar, J. Berger, T. Hanks, and J. Brune (1986). Rupture characteristics and tomographic source imaging of $M_l \approx 3$ earthquakes near Anza, Southern California, *J. Geophys. Res.* **91,** 12633–12650.

Frankel, A. and L. Wennerberg (1989). Microearthquake spectra from the Anza, California, seismic network: site response and source scaling, *Bull. Seism. Soc. Am.* **79,** 581–609.

Guo, H., A. Lerner-Lam, S. E. Hough, and W. Menke (1995). Empirical Green's function analysis of Loma Prieta aftershocks, P. Reasenberg, (Editor), *U.S. Geol. Surv. Prof. Paper,* in press.

Hanks, T. (1981). The corner frequency shift, and earthquake source models, *Q. Bull. Seism. Soc. Am.* **71,** 597–612.

Hanks, T. (1982). f_{max}, *Bull. Seism. Soc. Am.* **72,** 1869–1879.

Hanks, T. and D. Boore (1984). Moment-magnitude relations in theory and practice, *J. Geophys. Res.* **89,** 6229–6235.

Hartzell, S. (1989). Comparison of seismic waveform inversion results for the rupture history of a finite fault: application to the 1986 North Palm Springs, California, earthquake, *J. Geophys. Res.* **94,** 7515–7534.

Hauksson, E., L. M. Jones, K. Hutton, and D. Eberhart-Phillips (1993). The 1992 Landers earthquake sequence—seismological observations, *J. Geophys. Res.* **98,** 19835–19858.

Hough, S. E., and L. Seeber (1990). Seismological constraints on source properties of the m_b = 4.0 Ardsley, New York earthquake: a characteristic rupture? *J. Geophys. Res.* **96,** 18183–18195.

Hough, S. E., H. Guo, A. Lerner-Lam, L. Seeber, and C. Scholz (1992). Stress drop scaling: results from empirical Green's function analysis of Loma Prieta aftershocks (abstract), *Seism. Res. Lett.* **63,** 24.

Hough, S. E., J. Mori, E. Senbera, G. Glassmayer, C. Mueller, and S. Lydeer (1993). Southern surface rupture associated with the 1992 M7.4 Landers earthquake: did it all happen during the mainshock? *Geophys. Res. Lett.* **20,** 2615–2618.

Hough, S. E. and D. S. Dreger (1994). Observational constraints on earthquake source scaling? (abstract), *Trans. Am. Geophys. U.* **75,** 438.

Humphrey, J. R. and J. G. Anderson (1995). Seismic source parameters from the Guerrero subduction zone, *Bull. Seism. Soc. Am.* **84,** 1754–1769.

Hutchings, L. and F. Wu (1989). Empirical Green's functions from small earthquakes: a waveform study of locally recorded aftershocks of the 1971 San Fernando earthquake, *J. Geophys. Res.,* in press.

Kanamori, H., E. Hauksson, and T. Heaton (1991). TERRAscope and CUBE project at Caltech, *EOS. Trans. Am. Geophys. U.* **72,** 564.

Kanamori, H., J. Mori, E. Hauksson, T. H. Heaton, L. K. Hutton, and L. M. Jones (1993). Determination of earthquake energy release and ML using TERRAscope, *Bull. Seism. Soc. Am.* **83,** 330–346.

Lindley, G. T. (1994). Source parameters of the 23 April 1992 Joshua Tree, California, earthquake, its largest foreshocks, and aftershocks, *Bull. Seism. Soc. Am.* **84,** 1051–1057.

Lawson, C. L. and R. J. Hanson (1974). *Solving Least-Squares Problems,* Prentice-Hall, Englewood Cliffs, New Jersey.

Menke, W., L. Shengold, G. Hongsheng, H. Ge, and A. Lerner-Lam (1991). Performance of the short-period geophones of the IRIS/PASSCAL array, *Bull. Seism. Soc. Am.* **81,** 232–242.

Molnar, P., B. E. Tucker, and J. N. Brune (1973). Corner frequency of *P* and *S*-waves and models of earthquake sources, *Bull. Seism. Soc. Am.* **63,** 2091–2105.

Mori, J. and S. Frankel (1990). Source parameters for small events associated with the 1986 North Palm Springs, California, earthquake determined using the empirical Green's function method, *Bull. Seism. Soc. Am.* **80,** 278–295.

Mori, J. and S. Hartzell (1990). Source inversion of the 1988 Upland earthquake: determination of a fault plane for a small event, *Bull. Seism. Soc. Am.* **80,** 507–518.

Mori, J. and L. M. Jones (1992). Source characteristics and spatial clustering of the foreshocks to the Joshua Tree and Landers earthquakes (abstract), *Trans. Am. Geophys. U.* **73,** 393.

Mori, J. (1993). Fault plane determinations for three small earthquakes along the San Jacinto Fault, California: search for cross faults, *J. Geophys. Res.* **98,** 17711–17722.

Mori, J. (1994). Rupture directivity and slip distribution of the *M* 4.3 foreshock to the 1992 Joshua Tree earthquake, *Bull. Seism. Soc. Am.*, in press.

Mueller, C. S. (1985). Source pulse enhancement by deconvolution of an empirical Green's function, *Geophys. Res. Lett.* **12,** 33–36.

Singh, S. K. and M. Ordaz (1994). Seismic energy release in Mexican subduction zone earthquakes, *Bull. Seism. Soc. Am.* **84,** 1533–1550.

Urbancic and Young (1993). Space-time variations in source parameters of mining-induced seismic events with MLO, *Bull. Seism. Soc. Am.* **83,** 378–397.

Vernon, F. L. (1989). Analysis of data recorded at the Anza seismic network, *Ph.D. Thesis,* University of California, San Diego.

Xie, J., Z. Liu, R. B. Herrmann, and E. D. Cranswick (1991). Source parameters of three aftershocks of the 1983 Goodnow, New York, earthquake: High-resolution images of rupturing cracks, *Bull. Seism. Soc. Am.* **81,** 818–843.

U.S. Geological Survey
Pasadena, California 91106
(S.E.H.)

Seismographic Station
University of California
Berkeley, California 94720
(D.S.D.)

Manuscript received 1 September 1994.